



UNIVERSITY OF LEEDS

This is a repository copy of *Detection of terahertz frequency radiation via the photothermoelastic response of zinblend crystals*.

White Rose Research Online URL for this paper:  
<http://eprints.whiterose.ac.uk/78040/>

Version: Published Version

---

**Article:**

Dean, P, Awang, AH, Kundu, I et al. (6 more authors) (2013) Detection of terahertz frequency radiation via the photothermoelastic response of zinblend crystals. *Journal of the Optical Society of America B*, 30 (12). 12. 3151 - 3160. ISSN 0740-3224

<https://doi.org/10.1364/JOSAB.30.003151>

---

**Reuse**

Unless indicated otherwise, fulltext items are protected by copyright with all rights reserved. The copyright exception in section 29 of the Copyright, Designs and Patents Act 1988 allows the making of a single copy solely for the purpose of non-commercial research or private study within the limits of fair dealing. The publisher or other rights-holder may allow further reproduction and re-use of this version - refer to the White Rose Research Online record for this item. Where records identify the publisher as the copyright holder, users can verify any specific terms of use on the publisher's website.

**Takedown**

If you consider content in White Rose Research Online to be in breach of UK law, please notify us by emailing [eprints@whiterose.ac.uk](mailto:eprints@whiterose.ac.uk) including the URL of the record and the reason for the withdrawal request.



[eprints@whiterose.ac.uk](mailto:eprints@whiterose.ac.uk)  
<https://eprints.whiterose.ac.uk/>

# Detection of terahertz frequency radiation via the photothermoelastic response of zincblende crystals

Paul Dean,\* Aziati H. Awang, Iman Kundu, Raed Alhathloul, Suraj P. Khanna, Lianhe H. Li, Andrew Burnett, Edmund H. Linfield, and A. Giles Davies

*School of Electronic and Electrical Engineering, University of Leeds, Leeds LS2 9JT, UK*

*\*Corresponding author: p.dean@leeds.ac.uk*

Received August 23, 2013; accepted October 14, 2013;  
posted October 16, 2013 (Doc. ID 196162); published November 7, 2013

We present experimental evidence for a photothermoelastic response in zincblende crystals illuminated by quantum cascade laser sources in the frequency range 2.2–2.9 THz. Results obtained using an optically balanced sampling arrangement indicate a mechanism whereby the stress distribution established through localized heating of the crystal induces a change in optical birefringence via the photoelastic response of the crystal. A full mathematical model of this photothermoelastic mechanism in (110)-orientated crystals is presented, and shown to agree well with experimental measurements of the magnitude, and the orientational and spatial dependencies of the sampled signal in ZnTe and GaP crystals. © 2013 Optical Society of America

OCIS codes: (040.2235) Far infrared or terahertz; (140.5965) Semiconductor lasers, quantum cascade; (160.1190) Anisotropic optical materials; (350.5340) Photothermal effects.  
<http://dx.doi.org/10.1364/JOSAB.30.003151>

## 1. INTRODUCTION

The use of optically sampled crystals for the detection of terahertz (THz) frequency radiation has become widespread within applications such as THz time-domain spectroscopy (THz-TDS) [1–5]. The most commonly adopted detection scheme exploits the linear electro-optic (EO) (or Pockels) effect in noncentrosymmetric crystals whereby the THz field induces a birefringence in the crystal (typically ZnTe) that can be probed optically [6–9]. In addition to THz-TDS, EO sampling has similarly been applied to THz-pulsed imaging schemes employing both raster-scanning of the sample [10] and full-field CCD detection [10–12]. In each of these cases, and by virtue of the ultrafast timescales of the EO mechanism, the THz field can be sampled coherently using fs laser pulses that are synchronized with the THz emission [7].

EO crystals have more recently been applied to incoherent [13,14] and coherent sampling of THz fields generated using a quantum cascade laser (QCL) source. In the latter case, synchronization of the optical probe with the QCL has been accomplished by phase-seeding the QCL emission with THz pulses generated both externally [15] and internally [16] to the QCL cavity, as well as by electrical stabilization of the QCL using a phase-locked loop [17]. The use of these coherent EO sampling schemes has led to the study of active mode-locking [18], gain clamping [15], and more generally, the sampling coherence [19] of THz QCLs.

However, an alternative incoherent interaction mechanism between a ZnTe crystal and radiation from a THz QCL source has recently been demonstrated in a standard EO sampling arrangement [20]. Based on the dependence of the measured signal on the modulation frequency of the THz source, this previous study identified that this interaction has a thermal

origin. As such, this incoherent response was reported to be much slower than the picoseconds time response indicative of an EO mechanism such as that reported in [19]. Nevertheless, the specific mechanism of this thermal response was not established unequivocally in this previous study.

In this paper, we further investigate this interaction in ZnTe and GaP crystals illuminated by QCL sources in the frequency range 2.2–2.9 THz. We show that the measured response cannot be accounted for using the simple thermo-optic description proposed in [20], whereby the crystal refractive indices vary proportionally to the local temperature change. Rather, our results indicate a photothermoelastic origin whereby the stress distribution established through localized heating of the crystal induces a change in optical birefringence via the photoelastic response of the crystal. In addition to being of fundamental interest, an understanding of this incoherent interaction mechanism and its implications for EO sampling schemes is important for future studies involving THz QCLs as well as other THz sources.

This paper is organized as follows. In Section 2.A, we describe the experimental arrangement for optical sampling of the thermally induced birefringence in noncentrosymmetric crystals. Measurements of the response obtained from ZnTe crystals, under illumination by QCL sources emitting in the range 2.2–2.9 THz, are then presented in Section 2.B. In Section 2.C, we develop a simple model to describe the thermal response of these crystals to the absorption of THz radiation, and relate this to the measurements obtained. It is shown that the measured response cannot be fully accounted for using a simple thermo-optic model. In Section 3.A, a full model of the photothermoelastic response

of zincblende crystals to THz illumination is presented. Measurements of the magnitude and spatial dependence of the sampled signal are shown to agree well with the predictions of this model for ZnTe and GaP crystals, in Sections 3.B and 3.C, respectively. Finally, the possible presence of a thermally induced EO response in zincblende crystals is briefly discussed in Section 4, before conclusions are drawn in Section 5.

## 2. INVESTIGATION OF THERMALLY INDUCED BIREFRINGENCE IN ZINC TELLURIDE

### A. Experimental Arrangement

Figure 1(a) shows a schematic diagram of the experimental apparatus, which is based on a standard balanced electro-optic sampling arrangement [7]. In this study, three separate QCL devices were used: two bound-to-continuum (BTC) QCLs [21] tailored to emit at 2.2 and 2.6 THz, and a 2.9 THz QCL based on BTC active region with a phonon extraction/injection stage [22]. Each of the three devices was processed into a 150- $\mu\text{m}$ -wide semi-insulating surface plasmon ridge waveguide with lengths 4.5, 3, and 4.6 mm, respectively. The devices were cooled to  $\sim 25$  K using a helium-cooled continuous-flow cryostat and the THz radiation was collimated, passed through a rotatable wire-grid polarizer, and focused onto the detector crystal using parabolic reflectors. The focused spot sizes on the crystal were measured to be  $\sim 395$ ,  $\sim 330$ , and  $\sim 340$   $\mu\text{m}$  for the 2.2, 2.6, and 2.9 THz devices, respectively. Three crystals were investigated in this work, namely a wedged (110) ZnTe crystal with thickness  $L \sim 1.9$  mm, a 0.5-mm-thick (110) ZnTe crystal, and a 1-mm-thick (110) GaP crystal. QCL devices were driven either in continuous-wave, employing mechanical modulation, or in pulsed mode with 100 kHz pulse trains electrically modulated in the range 10–4 kHz, with lock-in detection of the photodiode output in both cases used to improve the detection sensitivity.

The crystal was optically sampled using the combined beams from two external cavity diode lasers at 778.3 nm, providing a combined power of  $\sim 20$  mW. The use of two lasers in this experiment is solely to provide greater optical power. Control of the polarization direction of the combined beams was achieved using a rotatable Glan–Thompson

polarizer, with a rotatable half-wave plate being used in each of the individual beams to maximize the power delivered to the crystal. The diode lasers were focused onto the crystal collinearly with the THz beam and a balanced sampling arrangement was used. Initially, the polarization of the sampling beam and THz beam were set to be parallel to the  $[-1, 1, 0]$  direction of the crystal, giving  $\theta = 0$  [see Fig. 1(b)]. The sampling position of the probe beam relative to the THz beam was adjusted to give the maximum response on the balanced photodiodes.

### B. Optical Sampling of Birefringence

In a standard EO sampling arrangement [7], the ellipticity of a linearly polarized near-infrared probe beam is modified by the optical anisotropy induced in a detector crystal by THz radiation. The relative phase delay  $\delta$  between the orthogonal polarization components of the probe beam that result from this birefringence is obtained by integrating along the beam propagation axis,

$$\delta = \int_0^L \frac{2\pi\Delta n(x)dx}{\lambda}. \quad (1)$$

Here,  $\lambda$  is the probe beam wavelength and  $L$  the crystal thickness. This phase delay is typically sampled using either a crossed polarizer and photodiode arrangement [23] or a quarter-wave plate, Wollaston prism, and pair of balanced photodiodes [7] [see Fig. 1(a)]. The dependence of the balanced photodiode signal on the orientation of the crystal relative to the THz electric field, as well as the orientation of the probe beam polarization has been described elsewhere [24] for the case of a (110)-cut cubic crystal with point group  $-43m$ , in which the optical anisotropy is induced through the EO response. This analysis can also be applied to the generalized case of optically sampling a refractive index ellipsoid, whose origin may not be EO, but whose major axis is orientated at an angle  $\alpha$  to the  $[-1, 1, 0]$  direction. The final expression for the balanced signal  $\Delta I$  in terms of the phase delay and probe intensity  $I_p$  is

$$\Delta I = I_p \sin(2(\alpha - \theta)) \cos(2\theta) \sin(\delta), \quad (2)$$

in which the factor  $\cos(2\theta)$  accounts for the more general case of the incident probe beam polarization being orientated at an

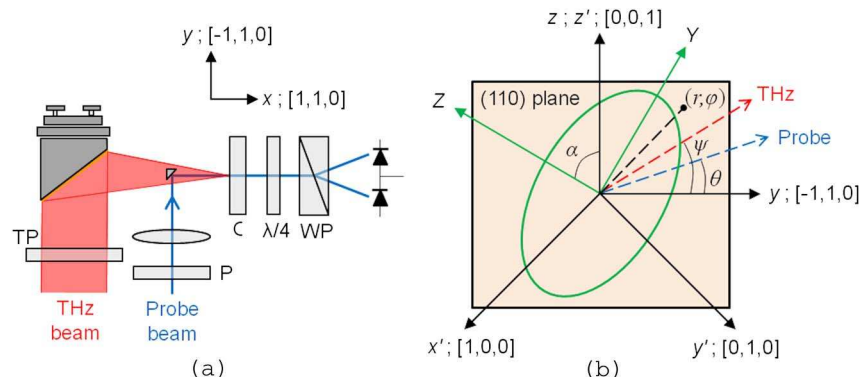


Fig. 1. (a) Experimental apparatus for optical sampling of the birefringence induced in a crystal by THz radiation. C, crystal;  $\lambda/4$ , quarter-wave plate; WP, Wollaston prism; P, optical polarizer; TP, THz polarizer. (b) Geometry of the (110) zincblende crystal showing the crystallographic axes ( $x'$ – $y'$ – $z'$ ), the Cartesian ( $y$ – $z$ ), and cylindrical ( $r$ ,  $\varphi$ ) axes in the (110) plane of the crystal, and the principal axes of the index ellipsoid ( $Y$ – $Z$ ). The  $x'$  and  $y'$  directions are bisected by the normal to the page. All other axes shown are in the plane of the page. Also shown are the angles  $\psi$  and  $\theta$  of the polarization directions of the THz and probe beams relative to the  $[-1, 1, 0]$  direction.

angle  $\theta$  to the polarization axis of the Wollaston prism, which in turn is defined as being parallel to the  $[-1, 1, 0]$  direction of the crystal [see Fig. 1(b)].

For the experimental arrangement described in Section 2.A, the phase delay can be inferred from the measured photodiode signal using Eq. (2) with  $\theta = 0$  and  $\alpha = \pi/4$ . Figure 2(a) shows the phase delays obtained using each of the three QCL devices with the  $\sim 1.9$  mm ZnTe crystal, and also for the 0.5 mm ZnTe crystal with the 2.2 THz laser. For these measurements the QCL powers were set to be approximately equal and were measured using a THz power meter to be 845, 800, and 805  $\mu\text{W}$  for the 2.2, 2.6, and 2.9 THz lasers, respectively. As can be seen, the measured response decreases with modulation frequency and tends toward an inverse relationship at higher frequencies. A similar behavior has been observed previously [20] using a 3.2 THz QCL, and is symptomatic of a thermal mechanism [25]. By rotation of the wire grid polarizer it has also been confirmed that, after correction for the variation of the transmitted THz power arising from the elliptically polarized QCL output, the measured phase delay is independent of the polarization direction  $\psi$  of the THz field. This is as expected for a thermal mechanism, and in agreement with observations reported elsewhere [20].

### C. Simple Thermal Model and Analysis

In order to characterize the optically sampled signal it is necessary first to evaluate the temperature increase arising from local heating of a crystal under THz illumination.

We consider the case of a THz beam of radius  $w_0$  incident on a crystal of density  $\rho$  and specific heat capacity  $C$ . The modulated THz power at a depth  $x$  below the crystal surface is assumed to take the form  $P = (1 - R)P_0 e^{-\alpha x} e^{i\omega t}$ , where  $\alpha$  is the absorption coefficient,  $R$  is the Fresnel reflection coefficient,  $P_0$  is the incident power and  $\omega$  is the modulation frequency. From conservation of energy we arrive at the heat equation for the temperature rise  $T(x, t)$

$$\rho C \pi w_0^2 \frac{dT(x, t)}{dt} = (1 - R)\alpha P_0 e^{-\alpha x} - GT(x, t). \quad (3)$$

Here,  $G$  is the thermal conductance per unit thickness of crystal, and the third term accounts for heat conduction radially away from the irradiated volume, although any radial temperature variation within this volume has been neglected for

simplicity. Heat conduction along the  $x$  direction has also been neglected in this model, since the probe beam samples the cumulative phase delay incurred along this direction [see Eq. (1)]. It is also assumed that there is negligible radiation into free space. The steady-state solution to Eq. (3) is  $T(x, t) = T(x)e^{i\omega t}$ , which by substitution gives the amplitude of the temperature modulation

$$\Delta T(x) = \frac{(1 - R)\alpha P_0 e^{-\alpha x}}{\sqrt{G^2 + (\rho C \pi w_0^2 \omega)^2}}. \quad (4)$$

This relation is characteristic of the Lorentzian frequency response of a thermal detector [25] and reduces to an inverse relationship between  $\Delta T(x)$  and  $\omega$  at high modulation frequencies.

In the simple thermo-optic model [20,26] it was assumed that this temperature modulation gives rise to a modulation of the optical birefringence  $\Delta n$  through the linear relation

$$\Delta n(x) = \beta \Delta T(x). \quad (5)$$

The validity of this relation will be further discussed in Section 3. In fact, it will be shown that the coefficient  $\beta$  is spatially inhomogeneous in the  $y$ - $z$  plane of the crystal by virtue of the spatial distribution of the THz beam intensity and the resulting stress distribution established in the crystal through spatially inhomogeneous local heating. Nevertheless, for a given sampling position on the crystal, the simple model described by Eqs. (4) and (5) can be used to quantify the variation of optical birefringence in terms of material parameters and the THz power, modulation frequency, and spot size.

In the present case of a thermally induced birefringence, the phase delay  $\delta$  can be obtained by applying Eqs. (1), (4), and (5) to give the result

$$\delta = \frac{2\pi\beta(1 - R)(1 - e^{-\alpha L})P_0}{\lambda \sqrt{G^2 + (\rho C \pi w_0^2 \omega)^2}}, \quad (6)$$

which can be expressed in terms of the temperature modulation at the crystal surface as

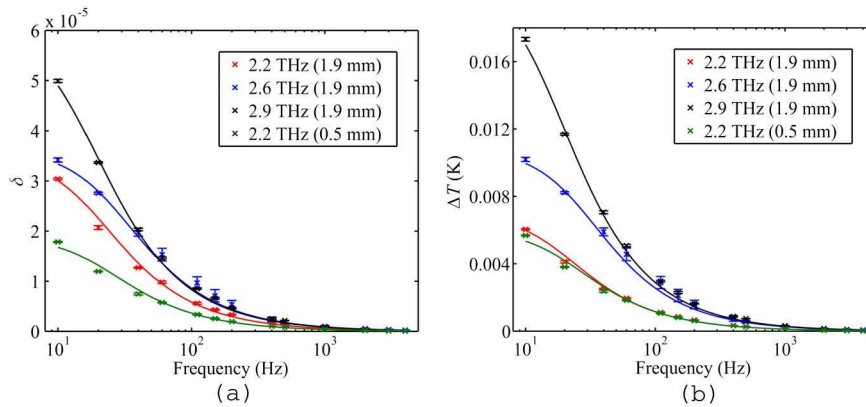


Fig. 2. (a) Phase delays measured as a function of modulation frequency for a  $\sim 1.9$  mm-thick ZnTe crystal, using QCL devices emitting at 2.2 THz (red), 2.6 THz (blue), and 2.9 THz (black), and also for a 0.5 mm ZnTe crystal at 2.2 THz (green). The error bars have been calculated based on three repeated measurements. The solid lines are fits to Eq. (6). (b) Corresponding temperature modulation at the crystal surface predicted using Eq. (7).

$$\delta = \frac{2\pi\beta(1 - e^{-\alpha L})}{\alpha\lambda} \Delta T(0). \quad (7)$$

Thus, through Eq. (6) the measured phase delay can be used to obtain the coefficient  $\beta$ .

Figure 2(a) shows fits of the data to Eq. (6), in which the values  $\beta$  and  $G$  are treated as free parameters. The absorption coefficients and Fresnel reflection coefficients used in these fits were obtained using THz-TDS, with  $\alpha$  being found to increase from  $15 \text{ cm}^{-1}$  at 2.2 THz to  $31 \text{ cm}^{-1}$  at 2.9 THz. As such, the factor  $(1 - e^{-\alpha L}) \approx 1$  for the crystal with  $L \sim 1.9 \text{ mm}$ , indicating almost complete absorption of the THz radiation at all three frequencies. Similarly, only  $\sim 47\%$  is absorbed in the case of the 0.5 mm crystal at 2.2 THz, which gives rise to the smaller optical phase delay observed. For ZnTe the value  $\rho C = 1.54 \text{ Jcm}^{-3} \text{ K}^{-1}$  was also used [27]. The fits are seen to agree well with the measured data and yield the average values  $\beta = 1.1 \times 10^{-6} \text{ K}^{-1}$  and  $G = 77 \text{ Wm}^{-1} \text{ K}^{-1}$ . As a matter of interest, the data can also be expressed in terms of the amplitude of temperature modulation at the crystal surface predicted via Eq. (7). This is shown in Fig. 2(b) and reveals temperature rises on the order of  $\sim 10 \text{ mK}$  at low modulation frequencies for the experimental conditions described here.

#### D. Analysis Based on Simple Thermo-Optic Model

One mechanism proposed to explain the origin of the observed modulation of optical birefringence is through a simple temperature dependence of the refractive indices [20]. Under this model the modulation of the birefringence can be expressed in terms of the temperature modulation according to Eq. (5) in which the coefficient  $\beta$  is given by

$$\beta \approx \left( \frac{JF + HF^2}{2} \right) \left( \frac{n_2 - n_3}{n_2 n_3} \right), \quad (8)$$

in which  $n_2$  and  $n_3$  are the refractive indices of the two principal axes of the crystal. As described elsewhere [28],  $J$  (defined as  $G$  in [20] and [28]) and  $H$  are optical constants relating to the thermal expansion coefficient and the temperature coefficient of the excitonic band gap, respectively, and  $F$  is related to both the sampling wavelength and the isentropic band gap lying in the UV region. Values of  $J$ ,  $H$  and the isentropic band gap have not been reported previously for ZnTe, although these are known for CdTe [28]. In order to evaluate Eq. (8), though, it is also necessary to obtain the “residual” birefringence  $n_2 - n_3$  induced by strain naturally present in the crystal in the absence of THz radiation [23].

Briefly, and following the analysis in [23], the signal obtained in a crossed sampling arrangement with no THz radiation, and with the wave plate adjusted (in the absence of the crystal) to give minimum signal transmitted through the crossed-polarizer, is given by

$$I = I_p \left( \eta + \sin^2 \left( \frac{\delta_0}{2} \right) \right), \quad (9)$$

in which  $\eta$  is the contribution to the photodiode signal arising from optical scattering. The residual phase delay  $\delta_0$  can be compensated using a correctly adjusted quarter-wave plate, which minimizes the transmitted intensity to the value  $I = \eta I_p$ , thereby enabling the scattering contribution in

Eq. (9) to be evaluated. A value  $\eta = 5.8 \times 10^{-4}$  is obtained from our measurements for the  $L \sim 1.9 \text{ mm}$  ZnTe crystal. Conversely, the transmitted signal can be maximized by adjusting the wave plate orientation, as in a balanced sampling configuration, to give a photodiode response  $I \approx I_p/2$  (since  $\eta \ll 1$ ). Using this value of  $I_p$  in Eq. (9) allows  $\delta_0$  to be estimated, from which the birefringence  $n_2 - n_3 = \delta_0 \lambda / 2\pi L = 4.3 \times 10^{-6}$  is obtained. Inserting this value into Eq. (8) with  $J = -9.2 \times 10^{-5} \text{ K}^{-1}$ ,  $H = 6.0 \times 10^4 \text{ K}^{-1}$ ,  $F = 1.8$  [28], and  $n_2 \approx n_3 = 2.86$  [29] yields  $\beta = 4.7 \times 10^{-10} \text{ K}^{-1}$ . This value predicted by the thermo-optic model is several orders of magnitude smaller than that observed experimentally, which indicates that the measured response does not arise principally from the simple thermo-optic mechanism proposed through Eq. (8). This will be further demonstrated in Section 3.B through measurements of the spatial inhomogeneity of the signal.

### 3. PHOTOTHERMOELASTIC EFFECT IN ZINCLENDE CRYSTALS

#### A. Theory of Photothermoelastic Effect

We next consider the presence of a photothermoelastic modulation of the optical birefringence in zincblende crystals under THz illumination. Such a response may be present owing to the thermal stresses induced in the crystal by localized heating. To evaluate this stress distribution we make use of the model developed for the case of an isotropic thin disk subject to a radial temperature distribution  $\Delta T(r, x)$ , where  $r$  is the radial coordinate. The radial  $\sigma_{rr}$  and tangential  $\sigma_{\varphi\varphi}$  components of the thermally induced stress are given as [30]

$$\sigma_{rr}(r, x) = \alpha_{\text{th}} Y \left[ \frac{1}{b^2} \int_0^b \Delta T(r', x) r' dr' - \frac{1}{r^2} \int_0^r \Delta T(r', x) r' dr' \right] \quad (10)$$

and

$$\sigma_{\varphi\varphi}(r, x) = \alpha_{\text{th}} Y \left[ \frac{1}{b^2} \int_0^b \Delta T(r', x) r' dr' + \frac{1}{r^2} \int_0^r \Delta T(r', x) r' dr' - \Delta T(r', x) \right], \quad (11)$$

in which  $Y$  is Young’s modulus,  $\alpha_{\text{th}}$  is the linear thermal expansion coefficient (which is isotropic in the case of cubic crystals [31]), and  $b$  is the disk radius. The faces of the disk are assumed to be unconstrained, giving a zero axial stress component. For the case of a Gaussian radial temperature distribution, inspection of Eqs. (10) and (11) reveal that the radial stress is everywhere compressive whereas the tangential stress component changes from compressive in the center of the disk to a tensile stress beyond a certain critical radius. We project the radial and tangential components of the second rank stress tensor onto the Cartesian laboratory axes  $y-z$  [see Fig. 1(b)] using the standard tensor transformations [32]. Owing to symmetry its components can be expressed in single suffix (matrix) notation as

$$\begin{pmatrix} \sigma_1 \\ \sigma_2 \\ \sigma_3 \\ \sigma_4 \\ \sigma_5 \\ \sigma_6 \end{pmatrix} = \begin{pmatrix} 0 \\ \sigma_{rr} \cos^2(\varphi) + \sigma_{\varphi\varphi} \sin^2(\varphi) \\ \sigma_{rr} \sin^2(\varphi) + \sigma_{\varphi\varphi} \cos^2(\varphi) \\ (\sigma_{rr} - \sigma_{\varphi\varphi}) \sin(\varphi) + \cos(\varphi) \\ 0 \\ 0 \end{pmatrix}, \quad (12)$$

in which the matrix components are related to the tensor components according to the standard conventions [31,32]: 1↔11; 2↔22; 3↔33; 4↔23, 32; 5↔13, 31; 6↔12, 21.

For a crystal of any symmetry a stress field will induce a perturbation to the refractive indices via the photoelastic mechanism [31]. This effect can be described in terms of the perturbation to the optical indicatrix according to

$$\Delta B_i = p_{ij} s_{jk} \sigma_k, \quad (13)$$

where  $p_{ij}$  are the components of the fourth-order photoelastic tensor and  $s_{ij}$  are the components of the fourth-order elastic compliance tensor in matrix notation. The matrices  $p_{ij}$  and  $s_{ij}$  can be calculated for the case of a (110) crystal through rotation of the matrices  $p'_{ij}$  and  $s'_{ij}$  corresponding to the crystallographic coordinate system (see Appendix A). Applying Eqs. (A7), (A16), and (12) to Eq. (13), and imposing the condition that the axial strain  $s_{1k} \sigma_k = 0$  for free expansion along the (110) direction, gives the result

$$\begin{pmatrix} \Delta B_1 \\ \Delta B_2 \\ \Delta B_3 \\ \Delta B_4 \\ \Delta B_5 \\ \Delta B_6 \end{pmatrix} = \begin{pmatrix} \sigma_2(p_{12}s_{11} + p_{13}s_{13}) + \sigma_3(p_{12}s_{13} + p_{13}s_{33}) \\ \sigma_2(p_{11}s_{11} + p_{13}s_{13}) + \sigma_3(p_{11}s_{13} + p_{13}s_{33}) \\ \sigma_2(p_{13}s_{11} + p_{33}s_{13}) + \sigma_3(p_{13}s_{13} + p_{33}s_{33}) \\ \sigma_4 p_{44} s_{44} \\ 0 \\ 0 \end{pmatrix}. \quad (14)$$

The optical indicatrix ellipsoid under the applied stress field thus becomes

$$x^2 \left( \frac{1}{n_1^2} + \Delta B_1 \right) + y^2 \left( \frac{1}{n_2^2} + \Delta B_2 \right) + z^2 \left( \frac{1}{n_3^2} + \Delta B_3 \right) + 2yz \Delta B_4 = 1. \quad (15)$$

The presence of the mixed term in Eq. (15) indicates that the main axes of the ellipsoid do not coincide with the  $y$ - $z$  axes. In order to evaluate the optical birefringence experienced by the probe beam as it passes through the crystal we must therefore identify a coordinate system that aligns with this ellipsoid. By inspection we note this can be accomplished by a rotation about the  $x$  axis [the (110) direction] through an angle  $\alpha$  given by

$$\tan(2\alpha) = \frac{2\Delta B_4}{\Delta B_2 - \Delta B_3}. \quad (16)$$

Thus, the new coordinate system  $X$ - $Y$ - $Z$  that aligns with the axes of the ellipsoid [Fig. 1(b)] is related to the crystallographic axes through the relations

$$x = X, \quad (17)$$

$$y = Y \cos(\alpha) - Z \sin(\alpha), \quad (18)$$

$$z = Z \cos(\alpha) + Y \sin(\alpha). \quad (19)$$

Substitution of Eqs. (17)–(19) into Eq. (15) gives the transformed equation for the ellipsoid

$$\begin{aligned} X^2 \left[ \frac{1}{n_1^2} + \Delta B_1 \right] + Y^2 \left[ \left( \frac{1}{n_2^2} + \Delta B_2 \right) \cos^2(\alpha) \right. \\ \left. + \left( \frac{1}{n_3^2} + \Delta B_3 \right) \sin^2(\alpha) + 2\Delta B_4 \sin(\alpha) \cos(\alpha) \right] \\ + Z^2 \left[ \left( \frac{1}{n_2^2} + \Delta B_2 \right) \sin^2(\alpha) + \left( \frac{1}{n_3^2} + \Delta B_3 \right) \cos^2(\alpha) \right. \\ \left. + 2\Delta B_4 \sin(\alpha) \cos(\alpha) \right] = 1, \end{aligned} \quad (20)$$

whose minor and major axes lie along the  $Y$  and  $Z$  directions, respectively. To calculate the corresponding modulation of the indices experienced by the orthogonal components of the probe beam we use the differential relation  $\Delta n_i = -(n_i^3/2)\Delta(1/n_i^2)$ , where the subscripts  $i = 1, 2, 3$  relate to the  $X, Y$ , and  $Z$  axes, which gives the results

$$\begin{aligned} \Delta n_Y = -\frac{n^3}{2} [\Delta B_2 \cos^2(\alpha) + \Delta B_3 \sin^2(\alpha) \\ + 2\Delta B_4 \sin(\alpha) \cos(\alpha)], \end{aligned} \quad (21)$$

$$\Delta n_Z = -\frac{n^3}{2} [\Delta B_2 \sin^2(\alpha) + \Delta B_3 \cos^2(\alpha) - 2\Delta B_4 \sin(\alpha) \cos(\alpha)]. \quad (22)$$

The resulting modulation of the birefringence is therefore

$$\begin{aligned} \Delta n(r, x) = \Delta n_Y - \Delta n_Z \\ = \frac{-n^3}{2} \left[ \frac{(\Delta B_2 - \Delta B_3)^2}{2\Delta B_4} + 2\Delta B_4 \right] \sin(2\alpha), \end{aligned} \quad (23)$$

where use has been made of Eq. (16). It should be noted that in the above analysis  $\Delta B_i$  and hence  $\Delta n(r, x)$  are both functions of  $x$  due to attenuation of the THz power as the beam propagates through the crystal, as well as functions of the transverse position ( $y, z$ ) [or equivalently ( $r, \varphi$ ) in cylindrical coordinates] by virtue of the spatial distribution of the stress field described by Eq. (12). As such, it emerges that the optical birefringence induced through the photothermoelastic mechanism cannot be characterized fully using the simple model described by Eqs. (4) and (5). In order to account for this spatial distribution of the stress field properly, we model the THz intensity as a Gaussian beam,  $I_r(r, x) = (1 - R)(2P_0/\pi w_0^2) \exp(-2r^2/w_0^2) \exp(-ax)$ . By analogy with Eq. (4) the amplitude of the spatially dependent temperature modulation is then assumed to take the form

$$\Delta T(r, x) = \frac{2(1 - R)\alpha P_0 e^{-ax} e^{-2r^2/w_0^2}}{\sqrt{G^2 + (\rho C \pi w_0^2 \omega)^2}}. \quad (24)$$

Thus, we may model the balanced photodiode signal accordingly. The stress field tensor  $\sigma_i$  can be obtained from Eq. (12), making use of Eqs. (10), (11), and (24). These tensor components thereby enable calculation of the modulation of

the birefringence via Eq. (23), and by applying Eqs. (14) and (16). The total phase delay can then be obtained from Eq. (1), from which the balanced photodiode signal can be calculated using Eq. (2). An important characteristic of this signal is that it exhibits spatial inhomogeneity originating from both the radial stress distribution, arising from localized heating in the crystal, and also through the  $\alpha$ -dependence of Eq. (2), which accounts for the orientation of the indicatrix ellipsoid relative to the probe beam polarization. This spatial dependence is confirmed experimentally in the next section.

### B. Experimental Results and Analysis for ZnTe

The spatial inhomogeneity of the photothermoelastic signal was investigated experimentally using the experimental arrangement described in Section 2.C, with the 2.2 THz QCL and the  $\sim 1.9$  mm ZnTe crystal. For these measurements the QCL was driven in pulsed mode and electrically modulated at a frequency of 40 Hz. In order to adjust the position of the probe beam focus relative to the focused THz beam, the focusing lens was manually scanned in the plane perpendicular to the beam axes using translation stages, with the balanced photodiodes being realigned for each measurement. Figure 3(a) shows a contour plot of the photodiode signal  $\Delta I/I_p$  measured across an area of  $1.4 \text{ mm} \times 1.4 \text{ mm}$  using a step size of 0.2 mm in both  $y$  and  $z$  directions. For comparison the spatial variation of the photodiode signal, calculated using Eq. (2) as described in Section 3.A, for the same experimental conditions is shown in Fig. 3(b). For this calculation the following values of the photoelastic constants [33] and stiffness matrix components [27] have been used for ZnTe:  $p'_{11} = 0.144$ ,  $p'_{12} = 0.094$ ,  $p'_{44} = 0.046$ , and  $c'_{11} = 7.1 \times 10^{10}$  Pa,  $c'_{12} = 4.1 \times 10^{10}$  Pa,  $c'_{44} = 3.1 \times 10^{10}$  Pa. As can be seen, for both the theoretical prediction and experimental results, the sign of the signal alternates in adjacent quadrants of the crystal surface and reaches a maximum magnitude at a critical radius along the  $\varphi = \pm\pi/4$  diagonals. The intensity is also seen to vanish toward zero at the origin. This radial variation of the signal originates from the radial dependence of the factor  $(\sigma_{rr} - \sigma_{\varphi\varphi})$  appearing in Eq. (12), which exhibits its maximum magnitude at some critical radius beyond that at which the tangential component of the stress tensor becomes tensile ( $\sigma_{\varphi\varphi} > 0$ ), as described by Eq. (11). It should be noted that such a spatial dependence of the measured response would not arise through a simple temperature-dependence

of the refractive indices, as described by the simple thermo-optic model.

We may further validate the photothermoelastic model through comparison of the magnitude of the predicted modulation of the birefringence with that observed experimentally. As noted previously, the optical birefringence arising through the photothermoelastic mechanism cannot be described fully using the simple model described by Eqs. (4) and (5). Nevertheless, to aid comparison with the experimental results presented in Section 2.C, it is convenient to cast the birefringence  $\Delta n(r, x)$  in terms of  $\Delta T(x)$  defined by Eq. (4). In this case spatial-dependence of  $\Delta n(r, x)$  becomes absorbed into the coefficient  $\beta$ . Figure 4(a) shows the simulated modulation amplitude calculated using Eq. (23), as described in Section 3.A, and cast in terms of the spatially dependent coefficient  $\beta$ . Here, the value of the linear thermal expansion coefficient  $\alpha_{\text{th}} = 8 \times 10^{-6} \text{ K}^{-1}$  [27] has been used, and the Young's modulus for ZnTe has been obtained from the stiffness constants using the relation  $Y = (c'_{11} + 2c'_{12})(c'_{11} - c'_{12})/(c'_{11} + c'_{12})$  [31]. It can be seen that the modulation is greatest away from the center of the THz beam and exhibits local maxima at positions  $\varphi = m\pi/2$  on the crystal surface (i.e., along the  $y$  and  $z$  axes). It should thus be noted that, by suitable rotation of the probe beam polarization away from  $\theta = 0$ , the photodiode signal could attain a maximum at these positions of maximum birefringence. Nevertheless, for these positions the indicatrix component  $\Delta B_4 = 0$  and hence the main axes of the indicatrix ellipsoid become aligned with the probe beam polarization [i.e.,  $\alpha = m\pi/2$ , see Fig. 4(b)] for the case when  $\theta = 0$ , giving zero sampled signal. Conversely, at the position of maximum signal [see Fig. 3(b)], a value  $\beta = 3.2 \times 10^{-6} \text{ K}^{-1}$  is predicted by the model. This agrees well with the value  $\beta = 1.1 \times 10^{-6} \text{ K}^{-1}$  obtained experimentally at the position of maximum response, which further confirms the proposed photothermoelastic origin of the signal. The discrepancy between simulated and measured values could be attributed to a number of assumptions made in the theoretical model. First, the approximation was made that the THz beam and radial temperature distribution follow a Gaussian distribution. We note that any asymmetry in the THz beam would cause deviation from the radial and tangential stress components described by Eqs. (10) and (11), and therefore to the optically sampled birefringence. Furthermore, a simple proportional form was adopted in our thermal

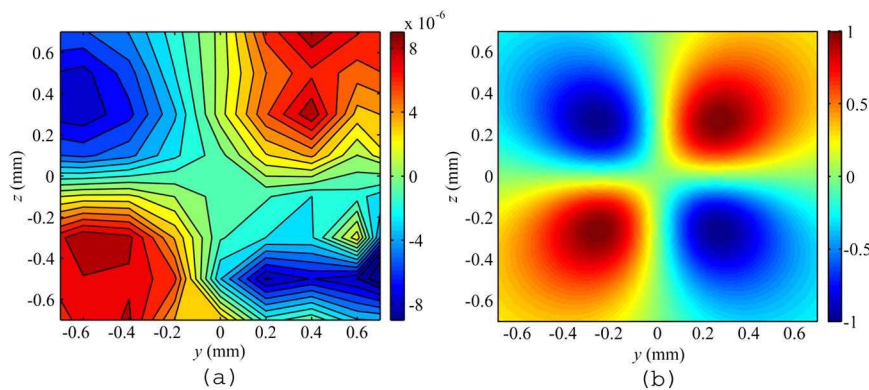


Fig. 3. (a) Contour plot showing the spatial variation of the photodiode signal  $\Delta I/I_p$  in the  $y$ - $z$  plane of the ZnTe crystal. The origin (0,0) corresponds to the center of the THz beam. For these measurements  $\theta = 0$  and the polarization direction of the THz field  $\psi = 0$ . (b) Spatial variation of the (normalized) photodiode signal calculated using the photothermoelastic model for the same experimental conditions.

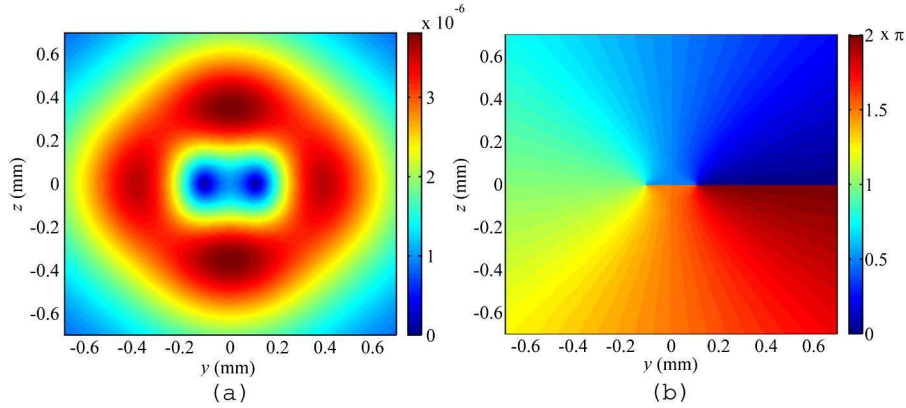


Fig. 4. (a) Spatial variation of the modulation of the birefringence in the  $y$ - $z$  plane of the ZnTe crystal, calculated using the photothermoelastic model and cast in terms of the coefficient  $\beta$  defined by Eq. (5). (b) Spatial variation of the angle  $\alpha$  obtained via Eq. (16). The origin (0,0) corresponds to the center of the THz beam.

model to describe the radial conduction of heat away from the irradiated volume, and axial heat conduction was neglected. The consequences of the latter assumption may be negligible, however, by virtue of the fact that the measured signal arises from the integration of the phase delay accumulated along the probe beam axis. A full numerical model of the temperature distribution within the crystal would nevertheless be feasible. Further discrepancies of the simulated response will have arisen due to uncertainties in the material parameters used, for example the photoelastic matrix components, which were taken from measurements at a slightly different optical wavelength of 633 nm.

As noted above, for the case of the probe beam polarization being aligned parallel to the  $[-1, 1, 0]$  direction of the crystal, the maximum measured response is observed at positions for which  $\varphi \approx \pm\pi/4, \pm3\pi/4$ . According to the photothermoelastic model the stress component  $\sigma_4$ , and hence  $\Delta B_4$ , attain maximum amplitudes in these cases and also  $\Delta B_2 \approx \Delta B_3$ . Therefore, at these positions of maximum response, the orientation of the ellipsoid is predicted to be  $\alpha \approx \pm\pi/4, \pm3\pi/4$  from Eq. (16). This can be verified experimentally by monitoring the photodiode signal for different orientations of the probe beam polarization  $\theta$ , with the quarter-wave plate being adjusted in each case to recover the a balanced signal in the absence of THz radiation. From Eq. (2) the optically sampled signal should then vary according to  $\Delta I \sim \cos^2(2\theta)$ . Figure 5 shows this measured response, and also a fit to an offset form of this functional dependence. The angular variation of the measured signal can be seen to agree well with that expected for the photothermoelastic response described.

### C. Experimental Results and Analysis for GaP

In order to evaluate the photothermoelastic model further, measurements were also performed using a 1-mm-thick (110) GaP crystal, which also belongs to the  $-43m$  point group. Figure 6 shows the phase delays measured using the 2.2 THz laser for electrical modulation frequencies in the range 10 Hz–3 kHz. For these measurements the same experimental procedure described in Section 2.C was used, with the sampling position of the probe beam again corresponding to the position of maximum response on the photodiodes. Figure 6 also shows a fit of the data to Eq. (6), in which the values  $\beta$  and  $G$  are treated as free parameters. In the case

of GaP, the following material parameters were used:  $\alpha = 4 \text{ cm}^{-1}$ ,  $R = 0.30$  (calculated from THz-TDS measurements), and  $\rho C = 1.78 \text{ Jcm}^{-3} \text{ K}^{-1}$  [34]. The fit is again seen to agree well with the measured data and yields the values  $\beta = 1.8 \times 10^{-6} \text{ K}^{-1}$  and  $G = 79 \text{ Wm}^{-1} \text{ K}^{-1}$ .

Using the same approach as described for ZnTe, the coefficient  $\beta$  can be quantitatively estimated at the position of maximum sampled signal using the photothermoelastic model. In this case a value  $\beta = 4.9 \times 10^{-6} \text{ K}^{-1}$  is predicted, which is again in good agreement with that measured. For this calculation the following values were used for GaP:  $p'_{11} = 0.161$ ,  $p'_{12} = 0.088$ ,  $p'_{44} = 0.073$ ;  $c'_{11} = 14.1 \times 10^{10} \text{ Pa}$ ,  $c'_{12} = 6.3 \times 10^{10} \text{ Pa}$ ,  $c'_{44} = 7.0 \times 10^{10} \text{ Pa}$  [35];  $\alpha_{\text{th}} = 4.7 \times 10^{-6} \text{ K}^{-1}$  [34]; and  $n = 3.20$  [36]. This predicted value also overestimates the measured result by a similar factor to that found for ZnTe, which can be explained by consideration of the approximations adopted in the photothermoelastic model, as discussed previously.

Whereas the coefficient  $\beta$  characterizes the photoelastic response of a crystal to a particular temperature distribution (or equivalently a particular stress field), the choice of sampling crystal will also influence the measured response through the

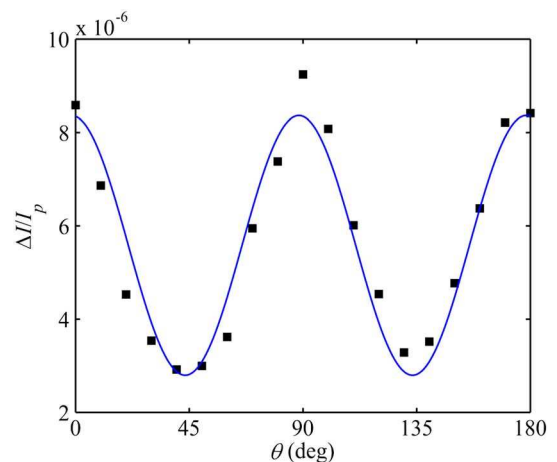


Fig. 5. Photodiode signal  $\Delta I/I_p$  (black squares) measured for different polarization directions  $\theta$  of the probe beam. Also shown (blue line) is the functional form  $\Delta I \sim \cos^2(2\theta)$ . These measurements were taken at the position corresponding to the maximum signal attained in Fig. 3(a), and with the polarization direction of the THz field  $\psi = 0$ .

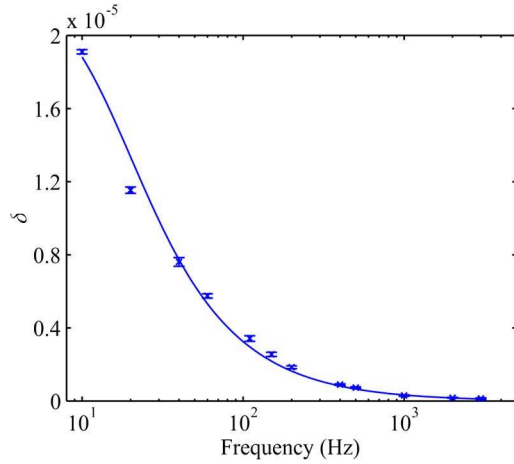


Fig. 6. Phase delays measured as a function of modulation frequency for a 1-mm-thick GaP crystal, using a QCL device emitting at 2.2 THz.

magnitude of the temperature modulation induced by the incident THz radiation, as well as the crystal thickness. We may define a figure-of-merit  $\mathcal{F}$  that determines the maximum measured response for a general (110)-orientated crystal with point group  $-43m$ . Retaining only the crystal physical parameters, and assuming a modulation frequency  $\omega \gg G/\rho C\pi w_0^2$ , we arrive at the relation

$$\mathcal{F} = \frac{\alpha_{th} Y n^3 p_{44} s_{44} (1 - e^{-\alpha L})}{\rho C}. \quad (25)$$

For ZnTe and GaP we obtain the values  $\mathcal{F} = 6.9 \times 10^{-12} \text{ J}^{-1} \text{ m}^3$  and  $3.0 \times 10^{-12} \text{ J}^{-1} \text{ m}^3$  at 2.2 THz, respectively. By comparison, the measured phase delays for these crystals are  $\alpha = 6.7 \times 10^{-7}$  and  $3.0 \times 10^{-7}$  at  $\omega = 1 \text{ kHz}$ , respectively, in good agreement with the ratio of the figures of merit.

#### 4. THERMALLY INDUCED ELECTRO-OPTIC EFFECT IN ZINCBLLENDE CRYSTALS

It is interesting to note that an additional incoherent mechanism for modulation of the optical birefringence under THz illumination may be present in the zincblende crystals considered in this work. It is known that cubic crystals do not exhibit primary pyroelectricity owing to their nonpolar crystal structure [31]. Nevertheless, a secondary pyroelectric response [31] may occur in noncentrosymmetric crystals under localized heating, whereby the thermally induced stress field results in an electric displacement through the piezoelectric response of the material. This in turn can induce a change in the optical birefringence through a linear (Pockels) EO effect, which is also exhibited by noncentrosymmetric crystals.

To estimate the magnitude of this response we start by calculating the electric displacement vector  $D_i$  arising from the piezoelectric response to the thermally induced stress field in the form [31,32]

$$D_i = d_{ij} \sigma_j. \quad (26)$$

For (110)-orientated crystals with point group  $-43m$  the only nonzero matrix components of the third-order piezoelectric tensor are  $d_{15} = -d_{24} = 2d_{31} = -2d_{32} = d'_{14}$ , where  $d'_{14}$  is

the piezoelectric strain coefficient [32]. Applying Eq. (12) gives the electric field components as

$$E_2 = -\frac{d'_{14}}{\epsilon} (\sigma_{rr} - \sigma_{\varphi\varphi}) \sin(\varphi) \cos(\varphi) \quad (27)$$

and

$$E_3 = -\frac{d'_{14}}{2\epsilon} [\sigma_{rr} \cos^2(\varphi) + \sigma_{\varphi\varphi} \sin^2(\varphi)], \quad (28)$$

where  $\epsilon$  is the permittivity. The resultant field magnitude  $E_T$  and its direction  $\psi_E$  relative to the (001)  $z$  axis are given by

$$E_T = \sqrt{E_2^2 + E_3^2}, \quad (29)$$

$$\tan(\psi_E) = \frac{-E_2}{E_3}. \quad (30)$$

The optical birefringence arising from the EO response to this electric field can be obtained following the analysis presented elsewhere [8,24]. The final modulation of the birefringence is found to be

$$\Delta n(r, x) = \frac{n^3 r_{41} E_T}{2} \sqrt{1 + 3 \sin^2(\psi_E)}, \quad (31)$$

in which  $r_{41}$  is the EO constant. In this case, the minor axis of the indicatrix ellipsoid is orientated at an angle  $\alpha$  relative to the  $[-1, 1, 0]$  direction given by

$$\tan(2\alpha) = -2 \tan(\psi_E). \quad (32)$$

The balanced photodiode signal can again be obtained from the birefringence through Eqs. (1) and (2). Figure 7 shows the spatial variation of this EO signal  $\Delta I/I_p$  calculated using the values  $d'_{14} = 0.9 \times 10^{-12} \text{ mV}^{-1}$  and  $r_{41} = 3.9 \times 10^{-12} \text{ mV}^{-1}$  [27] for ZnTe, in which the signal amplitude is shown on the same numerical scale as Fig. 3(b). As for the photothermoelastic case, this signal exhibits spatial inhomogeneity originating from both the radial stress distribution in the crystal and also through the geometrical dependence of the optical sampling

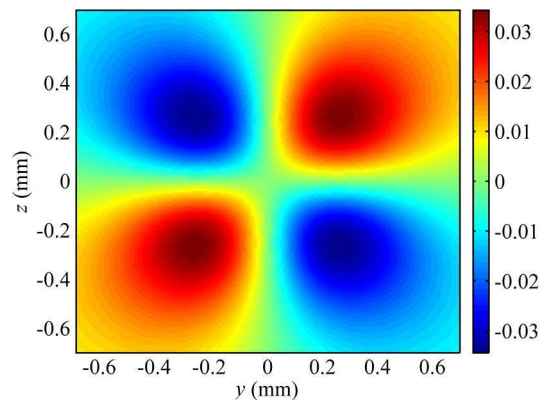


Fig. 7. Spatial variation of the photodiode signal  $\Delta I/I_p$  in the  $y$ - $z$  plane of the ZnTe crystal, calculated assuming only a thermally induced EO effect. The signal is displayed on the same numerical scale as Fig. 3(b).

described by Eq. (2). However, as can be seen, the EO signal magnitude is everywhere <4% that of the photothermoelastic signal, confirming that the latter is the dominant effect contributing to our measured response.

## 5. CONCLUSIONS

We have presented, for the first time, evidence of a photothermoelastic response in zincblende crystals under THz illumination. Using THz QCL sources emitting in the frequency range 2.2–2.9 THz, the optical birefringence induced in ZnTe and GaP crystals have been measured using a balanced sampling arrangement. The dynamic behavior of this response demonstrates a mechanism of thermal origin, although we have shown that the measured response cannot be accounted for using a simple thermo-optic description whereby the induced birefringence is proportional to the temperature rise in the crystal. Rather, our results indicate a photothermoelastic origin whereby the stress distribution established through localized heating of the crystal induces a change in optical birefringence via the photoelastic response of the crystal. A full mathematic model of this photothermoelastic mechanism in (110)-orientated zincblende crystals has been developed, and shown to agree well with experimental data. Specifically, measurements of the magnitude, and the orientational- and spatial-dependence of the sampled signal are found to agree well with the predictions of this model. In addition to being of fundamental interest, an understanding of this incoherent interaction mechanism and its implications for EO sampling schemes is important for future studies involving THz QCLs as well as other THz sources.

## APPENDIX A

Here we calculate the fourth-order photoelastic tensor  $P_{ijkl}$  and the fourth-order elastic compliance tensor  $S_{ijkl}$  in the laboratory coordinate system  $x-y-z$  [see Fig. 1(b)], for the case of a cubic crystal with point group  $-43m$ .

The 81 components of the fourth-order stiffness tensor  $C'_{ijkl}$  can be reduced to 36 components  $C'_{ij}$  in single suffix notation by noting that the symmetries  $C'_{ijkl} = C'_{klij} = C'_{jikl} = C'_{ijlk}$  apply. In addition, owing to symmetry considerations, only three components  $C'_{ij}$  are unique and nonzero for cubic crystals [31,32]. The stiffness matrix in the crystallographic coordinate system  $x'-y'-z'$  is given by

$$c' = \begin{pmatrix} c'_{11} & c'_{12} & c'_{12} & 0 & 0 & 0 \\ c'_{12} & c'_{11} & c'_{12} & 0 & 0 & 0 \\ c'_{12} & c'_{12} & c'_{11} & 0 & 0 & 0 \\ 0 & 0 & 0 & c'_{44} & 0 & 0 \\ 0 & 0 & 0 & 0 & c'_{44} & 0 \\ 0 & 0 & 0 & 0 & 0 & c'_{44} \end{pmatrix}, \quad (\text{A1})$$

from which the compliance matrix  $s' = [c']^{-1}$  may be calculated as

$$s' = \begin{pmatrix} s'_{11} & s'_{12} & s'_{12} & 0 & 0 & 0 \\ s'_{12} & s'_{11} & s'_{12} & 0 & 0 & 0 \\ s'_{12} & s'_{12} & s'_{11} & 0 & 0 & 0 \\ 0 & 0 & 0 & s'_{44} & 0 & 0 \\ 0 & 0 & 0 & 0 & s'_{44} & 0 \\ 0 & 0 & 0 & 0 & 0 & s'_{44} \end{pmatrix}, \quad (\text{A2})$$

where

$$s'_{11} = \frac{c'_{11} + c'_{12}}{(c'_{11} - c'_{12})(c'_{11} + 2c'_{12})}, \quad (\text{A3})$$

$$s'_{12} = \frac{-c'_{12}}{(c'_{11} - c'_{12})(c'_{11} + 2c'_{12})}, \quad (\text{A4})$$

$$s'_{44} = \frac{1}{c'_{44}}. \quad (\text{A5})$$

The transformed compliance matrix  $s$  is given by the relation

$$s = Ns'M^{-1}, \quad (\text{A6})$$

where  $N$  and  $M$  are the Bond strain and stress transformation matrices, respectively [32]. In our case these matrices represent a rotation of 45 deg about the  $z$  axis, for which the final result is

$$s = \begin{pmatrix} s_{11} & s_{12} & s_{13} & 0 & 0 & 0 \\ s_{12} & s_{11} & s_{13} & 0 & 0 & 0 \\ s_{13} & s_{13} & s_{33} & 0 & 0 & 0 \\ 0 & 0 & 0 & s_{44} & 0 & 0 \\ 0 & 0 & 0 & 0 & s_{44} & 0 \\ 0 & 0 & 0 & 0 & 0 & s_{66} \end{pmatrix}, \quad (\text{A7})$$

where

$$s_{11} = \frac{(s'_{11} + s'_{12})}{2} + \frac{s'_{44}}{4}, \quad (\text{A8})$$

$$s_{12} = \frac{(s'_{11} + s'_{12})}{2} - \frac{s'_{44}}{4}, \quad (\text{A9})$$

$$s_{13} = s'_{12}, \quad (\text{A10})$$

$$s_{33} = s'_{11}, \quad (\text{A11})$$

$$s_{44} = s'_{44}, \quad (\text{A12})$$

$$s_{66} = 2(s'_{11} - s'_{12}). \quad (\text{A13})$$

Likewise, for cubic crystals, only three of the components  $p'_{ij}$  of the photoelastic matrix are unique and nonzero [31]

$$p' = \begin{pmatrix} p'_{11} & p'_{12} & p'_{12} & 0 & 0 & 0 \\ p'_{12} & p'_{11} & p'_{12} & 0 & 0 & 0 \\ p'_{12} & p'_{12} & p'_{11} & 0 & 0 & 0 \\ 0 & 0 & 0 & p'_{44} & 0 & 0 \\ 0 & 0 & 0 & 0 & p'_{44} & 0 \\ 0 & 0 & 0 & 0 & 0 & p'_{44} \end{pmatrix}. \quad (\text{A14})$$

The transformed photoelastic matrix  $p$  is given by the relation [32]

$$p = Mp'N^{-1}, \quad (\text{A15})$$

for which the final result is

$$p = \begin{pmatrix} p_{11} & p_{12} & p_{13} & 0 & 0 & 0 \\ p_{12} & p_{11} & p_{13} & 0 & 0 & 0 \\ p_{13} & p_{13} & p_{33} & 0 & 0 & 0 \\ 0 & 0 & 0 & p_{44} & 0 & 0 \\ 0 & 0 & 0 & 0 & p_{44} & 0 \\ 0 & 0 & 0 & 0 & 0 & p_{66} \end{pmatrix}, \quad (\text{A16})$$

where

$$p_{11} = \frac{(p'_{11} + p'_{12})}{2} + p'_{44}, \quad (\text{A17})$$

$$p_{12} = \frac{(p'_{11} + p'_{12})}{2} - p'_{44}, \quad (\text{A18})$$

$$p_{13} = p'_{12}, \quad (\text{A19})$$

$$p_{33} = p'_{11}, \quad (\text{A20})$$

$$p_{44} = p'_{44}, \quad (\text{A21})$$

$$p_{66} = \frac{(p'_{11} - p'_{12})}{2}. \quad (\text{A22})$$

## ACKNOWLEDGMENTS

We are grateful for support from EPSRC (UK), the Royal Society, the Wolfson Foundation, the European Research Council grant “NOTES,” and Universiti Teknologi MARA (UiTM).

## REFERENCES

- M. C. Nuss and J. Orenstein, *Millimeter and Submillimeter Wave Spectroscopy of Solids* (Springer, 1998).
- M. C. Beard, G. M. Turner, and C. A. Schmuttenmaer, “Terahertz spectroscopy,” *J. Phys. Chem. B* **106**, 7146–7159 (2002).
- C. A. Schmuttenmaer, “Exploring dynamics in the far-infrared with terahertz spectroscopy,” *Chem. Rev.* **104**, 1759–1780 (2004).
- A. G. Davies, A. D. Burnett, W. Fan, E. H. Linfield, and J. E. Cunningham, “Terahertz spectroscopy of explosives and drugs,” *Mater. Today* **11**(3), 18–26 (2008).
- P. Y. Han and X.-C. Zhang, “Free-space coherent broadband terahertz time-domain spectroscopy,” *Meas. Sci. Technol.* **12**, 1747–1756 (2001).
- Q. Wu and X.-C. Zhang, “Free-space electro-optic sampling of terahertz beams,” *Appl. Phys. Lett.* **67**, 3523–3525 (1995).
- Q. Wu and X. C. Zhang, “Ultrafast electro-optic field sensors,” *Appl. Phys. Lett.* **68**, 1604–1606 (1996).
- Q. Chen, M. Tani, Z. Jiang, and X.-C. Zhang, “Electro-optic transceivers for terahertz-wave applications,” *J. Opt. Soc. Am. B* **18**, 823–831 (2001).
- N. C. J. van der Valk, T. Wenckebach, and P. C. M. Planken, “Full mathematical description of electro-optic detection in optically isotropic crystals,” *J. Opt. Soc. Am. B* **21**, 622–631 (2004).
- Z. Jiang and X.-C. Zhang, “Terahertz imaging via electro-optic effect,” *IEEE Trans. Microw. Theory Tech.* **47**, 2644–2650 (1999).
- Q. Wu, T. D. Hewitt, and X. C. Zhang, “Two-dimensional electro-optic imaging of THz beams,” *Appl. Phys. Lett.* **69**, 1026–1028 (1996).
- M. Usami, M. Yamashita, K. Fukushima, C. Otani, and K. Kawase, “Terahertz wideband spectroscopic imaging based on two-dimensional electro-optic sampling technique,” *Appl. Phys. Lett.* **86**, 141109 (2005).
- R. Rungsawang, O. Marshall, J. R. Freeman, H. E. Beere, S. Malik, J. Alton, S. Barbieri, and D. A. Ritchie, “Intensity detection of terahertz quantum cascade laser radiation using electro-optic sampling,” *Appl. Phys. Lett.* **93**, 191111 (2008).
- J. Darmo, M. Martl, and K. Unterrainer, “Quasi phase-matched terahertz detector,” *Electron. Lett.* **46**, 788–790 (2010).
- D. Oustinov, N. Jukam, R. Rungsawang, J. Madéo, S. Barbieri, P. Filloux, C. Sirtori, X. Marcadet, J. Tignon, and S. Dhillon, “Phase seeding of a terahertz quantum cascade laser,” *Nat. Commun.* **1**, 1–6 (2010).
- J. Maysonnave, N. Jukam, M. S. M. Ibrahim, K. Maussang, J. Madéo, P. Cavalié, P. Dean, S. P. Khanna, D. P. Steenson, E. H. Linfield, A. G. Davies, J. Tignon, and S. S. Dhillon, “Integrated injection seeded terahertz source and amplifier for time-domain spectroscopy,” *Opt. Lett.* **37**, 731–733 (2012).
- S. Barbieri, P. Gellie, G. Santarelli, L. Ding, W. Mauneult, C. Sirtori, R. Colombelli, H. Beere, and D. Ritchie, “Phase-locking of a 2.7-THz quantum cascade laser to a mode-locked erbium-doped fibre laser,” *Nat. Photonics* **4**, 636–640 (2010).
- S. Barbieri, M. Ravano, P. Gellie, G. Santarelli, C. Manquest, C. Sirtori, S. P. Khanna, E. H. Linfield, and A. G. Davies, “Coherent sampling of active mode-locked terahertz quantum cascade lasers and frequency synthesis,” *Nat. Photonics* **5**, 306–313 (2011).
- J. Maysonnave, N. Jukam, M. S. M. Ibrahim, R. Rungsawang, K. Maussang, J. Madéo, P. Cavalié, P. Dean, S. P. Khanna, D. P. Steenson, E. H. Linfield, A. G. Davies, S. S. Dhillon, and J. Tignon, “Measuring the sampling coherence of a terahertz quantum cascade laser,” *Opt. Express* **20**, 16662–16670 (2012).
- A. van Kolck, M. Amanti, M. Fischer, M. Beck, J. Faist, and J. Lloyd-Hughes, “Thermo-optic detection of terahertz radiation from a quantum cascade laser,” *Appl. Phys. Lett.* **97**, 251103 (2010).
- S. Barbieri, J. Alton, H. E. Beere, J. Fowler, E. H. Linfield, and D. A. Ritchie, “2.9 THz quantum cascade lasers operating up to 70 K in continuous wave,” *Appl. Phys. Lett.* **85**, 1674–1676 (2004).
- M. I. Amanti, G. Scalari, R. Terazzi, M. Fischer, M. Beck, J. Faist, A. Rudra, P. Gallo, and E. Kapon, “Bound-to-continuum terahertz quantum cascade laser with a single-quantum-well phonon extraction/injection stage,” *New J. Phys.* **11**, 125022 (2009).
- Z. Jiang, F. G. Sun, Q. Chen, and X. C. Zhang, “Electro-optic sampling near zero optical transmission point,” *Appl. Phys. Lett.* **74**, 1191–1193 (1999).
- P. C. M. Planken, H.-K. Nienhuys, H. J. Bakker, and T. Wenckebach, “Measurement and calculation of the orientation dependence of terahertz pulse detection in ZnTe,” *J. Opt. Soc. Am. B* **18**, 313–317 (2001).
- R. A. Smith, F. E. Jones, and R. P. Chasmar, *The Detection and Measurement of Infrared Radiation*, 2nd ed. (Oxford University, 1968).
- V. S. Cherkassky, B. A. Knyazev, V. V. Kubarev, G. N. Kulipanov, G. L. Kuryshv, A. N. Matveenko, A. K. Petrov, V. M. Popik, M. A. Scheglov, O. A. Shevchenko, and N. A. Vinokurov, “Imaging techniques for a high-power THz free electron laser,” *Nucl. Instrum. Methods Phys. Res., Sect. A* **543**, 102–109 (2005).
- S. Adachi, *Handbook on Physical Properties of Semiconductors* (Kluwer Academic, 2004), Vol. **3**.
- G. Ghosh, “Temperature dispersion of refractive indices in semiconductors,” *J. Appl. Phys.* **79**, 9388–9389 (1996).
- M. Bass, *Handbook of Optics*, 3rd ed. (McGraw-Hill, 2009), Vol. **4**.
- B. A. Boley and J. H. Weiner, *Theory of Thermal Stresses* (Wiley, 1960).
- J. F. Nye, *Physical Properties of Crystals* (Clarendon, 1957).
- B. A. Auld, *Acoustic Fields and Waves in Solids*, 2nd ed. (Krieger, 1990), Vol. **1**.
- M. Yamada, K. Yamamoto, and K. Abe, “Elastic and photoelastic constants of ZnTe measured by Brillouin scattering,” *J. Phys. D* **10**, 1309–1313 (1977).
- M. E. Levinštejn, S. Romyantsev, and M. Shur, *Handbook Series on Semiconductor Parameters* (World Scientific, 1999), Vol. **2**.
- M. Yamada, K. Wasa, and C. Hamaguchi, “Brillouin scattering in GaP,” *Jpn. J. Appl. Phys.* **15**, 1107–1111 (1976).
- W. L. Bond, “Measurement of the refractive indices of several crystals,” *J. Appl. Phys.* **36**, 1674–1677 (1965).